Cavitation erosion of glass fibre reinforced polymer composites with unidirectional layup

Guobys, Raimondas; Rodriguez, Alvaro; Chernin, Leon

Published in:
Composites Part B: Engineering

DOI:
10.1016/j.compositesb.2019.107374

Publication date:
2019

Cavitation Erosion of Glass Fibre Reinforced Polymer Composites with Unidirectional Layup

R. Guobys*, Á. Rodríguez#, L. Chernin*†

* School of Science and Engineering, University of Dundee, Nethergate, Dundee, Scotland, DD1 4HN, UK
# Centro Tecnológico de Componentes (CTC), PCTCAN, Isabel Torres 1, 39011 Santander, Spain
† Corresponding author; Email: l.chernin@dundee.ac.uk; Tel: +44(0)1382 384922; Fax: +44(0)1382 384389

Abstract

Glass fibre reinforced polymer (GFRP) composites are increasingly used in marine applications and can be subjected to aggressive environmental effects, one of which is cavitation. This study investigates the behaviour of unidirectional GFRP composites exposed to cavitation erosion generated using an ultrasonic transducer. Cavitation erosion tests were performed in accordance with the ASTM G32 standard. All specimens were preconditioned to eliminate the influence of water absorption on the mass loss caused by cavitation. The erosion process was monitored with a microscope and the mass loss was measured at regular periods. The tested specimens were scanned with X-ray computed microtomography. The research findings indicated that the erosion process was affected by several parameters including specimen thickness, distance between fibre bundles, bundle shape and distribution. The initiation and development of erosion damage were highly influenced by the surface condition. Cavitation erosion traced parts of fibre bundles located closer to the surface creating trenches and valleys on the surface. The regions with thick epoxy layers above and between fibre bundles were much less susceptible to erosion damage. Several erosion mechanisms were identified and discussed. The research findings also highlighted the difficulties in characterising ultrasonic cavitation erosion of GFRP composites using acoustic impedance and mean erosion depth.

Keywords: Glass fibre reinforced polymer (GFRP) composites; Ultrasonic cavitation erosion; Surface analysis; X-ray microtomography (Micro-CT)

1. Introduction

Glass fibre reinforced polymer (GFRP) composites are widely used in the marine industry for manufacturing of blades of tidal stream turbine rotors and boat propellers. Interaction of the blades with seawater causes pressure variations on the blade surfaces. Under certain conditions, surface pressure can fall under the vapour pressure of water leading to the development of cavitation. Depending on the severity and extent, cavitation can lead to noise, vibrations, loss of efficiency and surface erosion. The erosion potential of one imploding cavitation bubble is very small. However, the accumulating erosive effect of the long-term exposure to cavitation clouds is so great that, currently, no known materials can withstand it. To date, very few research works have been done on the resistance of GFRP composites to cavitation erosion and the effect of the inner fibre/epoxy structure on the erosion performance.

Hammond et al. [1] investigated the resistance of fibre reinforced composites with epoxy matrix to cavitation erosion in artificial seawater. The authors used an ultrasonic transducer with the peak to peak amplitude of the transducer tip equal to 25 μm. Part of the specimens was conditioned in the salt water before testing, while the other part was tested from the dry state. The specimens had bi- and multidirectional fibre layups, both with a relatively uniform distribution of fibres per layer. The tests demonstrated higher erosion of specimen surfaces in the matrix region between fibres. The effect of epoxy inclusion size on the composite erosion performance was not studied though. It is important to note that the results of the tests on the dry specimens should be treated with caution. The chosen testing methodology could not prevent water absorption by the FRP specimens, and it would be difficult to take into account the effect of water absorption on the mass loss accurately.

Yamatogi et al. [2] eroded FRP specimens using an ultrasonic transducer with the 50 μm peak to peak amplitude. The specimens had bi- and multiaxial layups with fibre bundles bonded by

epoxy. The mass loss was measured using a filtration system with the finest mesh size of 0.45 μm. The captured eroded fragments consisted of both the epoxy and fibres, and strongly depended on fibre/epoxy bonding.

The present study reports the results of tests on unidirectional GFRP composites with epoxy matrix exposed to cavitation erosion. The specimens used in the tests were supplied by a manufacturer of tidal turbine blades. The surface hardness of specimens was characterised with a Shore Durometer Type D. The specimens were preconditioned in deionised water. Cavitation was generated by an ultrasonic transducer. The mechanics of surface erosion was studied using specimens with four different fibre bundle distributions and two specimen thickness groups. The erosion depth and rate were evaluated at different testing stages based on specimen mass loss. The erosion imprints were routinely analysed using a microscope and photographed. The generated test data was compared with the data from existing research studies. All specimens were scanned after testing by X-ray computed microtomography (Micro-CT). The obtained Micro-CT images were analysed with image processing software yielding detailed information about the erosion imprint topography and the internal fibre/epoxy structure of the composite specimens. The measured and photographic data generated during the tests was subjected to a vigorous, critical examination.

2. Material and experimental setup

2.1. Materials

16 GFRP composite specimens were cut out of four sheets with a target thickness of 2 and 4 mm and divided into two thickness groups. Each specimen was marked by two digits, where the first digit indicated the sheet number and the second the sample number from the sheet.

The GFRP composite sheets were manufactured using bidirectional non-crimp glass fabric with 0/90 layup and weight of 1171/39 g/m^2. The fibres were made of E-glass. The diameter

of a single fibre was 19 μm. The main bundles had most of the fibres in the fabric and were oriented in the 0° direction. The secondary bundles in the 90° direction had a very small volume fraction. The main and secondary bundles were stitched together with synthetic thread. The 2 mm thick specimens were composed of 2 laminae with 0/90 and 90/0 layups of the fabric, while the 4 mm thick specimens had 4 laminae with 3 × (0/90) and 90/0 layups. Therefore, the main bundles were always located at both specimen surfaces. In each sheet, the main bundles in all laminae were aligned in the same direction. Examples of bundle layups in specimens are depicted in Section 3.4. The laminae were bonded by epoxy using a vacuum assisted resin transfer moulding process. In this study, the GFRP composites were called 'unidirectional' because of two reasons. First, the main bundles were significantly larger than the secondary bundles and aligned in one direction in all laminae. Second, the erosion imprint did not reach the secondary bundles of the top lamina in any of the tests conducted (see Section 3.4).

All the specimens were scanned before testing by the X-ray computed microtomography (Micro-CT) system Nikon XT H 225 ST. The scans were analysed with the image processing software VGStudio Max [3]. The geometry, distribution and stacking of the fibre bundles were measured at different cross-sectional planes. The shapes of bundle cross-sections varied between an oval and a quadrilateral (parallelogram or rectangle) with rounded corners. The bundle cross-section of specimens from sheet 1 was equal to 2.37 mm (with standard deviation of $\sigma = 0.09$ mm) in width and 0.84 mm ($\sigma = 0.06$ mm) in height. The distances between bundles in a layer and between layers of bundles varied from 0 to 0.2 mm. In the sheets 2, 3 and 4, the bundle cross-sections were equal to 3.28 mm ($\sigma = 0.22$ mm) in width and 0.87 mm ($\sigma = 0.07$ mm) in height. The distance between bundles varied from 0 to 0.4 mm, while the distance between bundle layers varied from 0 to 0.2 mm.

The mechanical properties of the GFRP composite, which was manufactured and provided by ÉireComposites (see Acknowledgements), are given in Table 1.

Table 1. GFRP composite mechanical properties

	Strength (MPa)	Modulus (GPa)
Tensile 0	751.00	36.00
Tensile 90	52.00	11.00
Compression 0	747.20	38.10
Compression 90	175.90	11.30
In-plane shear	79.98	4.12
Flexure	786.37	34.50
Interlaminar Shear	65.74	-

The geometrical and material properties of specimens are presented in Table 2. As per manufacturer's specifications, the target GFRP composite density (ρ) was equal to 1910 kg/m^3, where the glass fibre density was equal to 2600 kg/m^3 and the epoxy matrix density to 1220 kg/m^3. The density of each specimen was calculated based on the measurements of dimensions and mass. It was observed that the density of the specimens differed by up to 3.9% from the target value. All specimens had square shapes with 50 mm sides. The surfaces of specimens had slight 'waviness'. The specimen thickness (t) between fibre bundles was smaller by 0.03 mm than that above the bundles, where the latter is given in Table 2. ISO 1172 method A [4] was used to measure the fibre volume fraction (FVF) in seven specimens: 13, 14, 23, 24, 33, 34 and 43. All the specimens demonstrated good consistency in the measured parameters.

The volume loss of polymeric materials has a good relationship with the Shore hardness (Böhm et al. [5]). The hardness of dry GFRP specimens was tested using Shore Durometer Type D, as per ASTM D2240 [6]. Since the surface of unidirectional GFRP composite is divided into zones above and between fibre bundles, two sets of measurement were performed

for each specimen. Table 2 includes the measurements of the Shore hardness above fibre bundles (S_B) and between bundles (S_E). The average S_B is equal to 92.4 HD and S_E is equal to 87.6 HD, which is 5.2% smaller. S_B is affected by the thickness of the epoxy layer covering bundles, while the variation of S_E is affected by the width of the epoxy between bundles. It is necessary to note that ASTM D2240 [6] states that measurement above 90 HD are not reliable. However, the obtained values provide a good indication of the stiffening effect of fibres on the composite surface. The cavitation erosion tests were conducted using deionised water. The prolonged saturation of specimens in water during preconditioning was found to have a negligible effect on GFRP surface hardness. The description of the preconditioning process is given in Section 2.2. The properties of the deionised water including the density, the speed of sound (v) and the acoustic impedance (z) are presented in Table 2.

The ultrasonic transducer induced vibration of specimens and heavy mixing of water in a beaker. To prevent the loss of material (damaged by specimen cutting) from edges during testing, the edges of all specimens were covered with epoxy. The density of the epoxy covering the edges was 1110 kg/m^3 (Resoltech resin 1050 and hardener 1058S). The epoxy was degassed in a vacuum chamber prior the application to minimise the volume fraction of cavities. The specimens were cured and conditioned in an oven at 50°C for 24 hours.

Two additional specimens made of Stainless Steel 316 (SS316) were used for calibration and comparative purposes. The density of SS316 was measured to be 7910 kg/m^3. Both specimens were cut to approximately 40 mm × 40 mm, with the thickness of 2.95 mm. The specimen surfaces were mirror polished before the cavitation erosion testing as per ASTM G32 [7].

Table 2. Measured properties of GFRP specimens and testing liquid

No.	t (mm)	m (g)	FVF (%)	ρ (kg/m^3)	v (m/s)	z (Pa·s/m ×10^6)	S_B (HD)	S_E (HD)
11	1.9	9.26	-	1910	2497	4.77	90.8	89.0
12	1.9	9.28	-	1910	2473	4.72	90.6	88.5
13	1.9	9.12	49.95	1909	2461	4.70	-	-
14	1.9	9.31	49.93	1909	2499	4.77	-	-
21	2.1	9.57	-	1847	2480	4.58	91.5	85.0
22	2.0	9.22	-	1847	2457	4.54	92.7	86.4
23	2.0	9.37	46.15	1857	2461	4.57	-	-
24	2.1	9.49	44.78	1838	2481	4.56	-	-
31	3.5	17.38	-	1947	2852	5.55	94.3	89.2
32	3.5	17.52	-	1947	2838	5.53	94.0	88.6
33	3.5	17.37	52.26	1941	2825	5.48	-	-
34	3.5	17.39	53.07	1952	2842	5.55	-	-
41	3.7	17.94	-	1910	2882	5.50	92.8	86.8
42	3.7	17.95	-	1910	2814	5.37	92.5	87.4
43	3.7	18.20	50.23	1913	2871	5.49	-	-
44	3.7	17.86	-	1910	2829	5.40	-	-
Water (at 23°C)				998	1490	1.49		

In Table 2: t is the specimen thickness; m is the specimen mass; FVF is the fibre volume fraction; ρ is the density; v is the speed of sound; z is the acoustic impedance; S_B and S_E are the Shore hardness of the GFRP specimen surface above and between fibre bundles, respectively.

Note: All the parameters presented in Table 2 were measured by the researchers.

2.2. Cavitation erosion test and measurements

Cavitation erosion tests on stationary specimen were conducted in accordance with the ASTM G32 [7] standard. The specimens were submerged 12 mm below the liquid surface in a beaker filled with deionised water (850 mL in volume). The specimen displacement was prevented in all directions. The deionised water conductivity was kept under 1 µS/cm throughout testing. To maintain temperature at 25 ± 2°C, the deionised water was replaced during each routine pause in the cavitation erosion testing for measurements. The temperature was monitored

locally at the eroded specimen surface with a precision of ±0.1°C before and after specimen surface erosion.

GFRP composites tend to absorb moisture [8-14], which can prevent measuring the mass loss during cavitation erosion tests accurately. Three first erosion tests were carried out on control specimens without preconditioning in water. This led to a mass gain in all specimens during an initial stage of erosion testing due to water absorption (e.g., 5.2 mg was gained just after 15 minutes of initial erosion at the 25 μm peak to peak amplitude). Therefore, the main batch of specimens was preconditioned by submerging in deionised water with conductivity of <1 μS/cm until the moisture equilibrium was reached (following procedures of ASTM D5229/D5229M [15] and ASTM D570 [16] standards). In the preconditioning process, all specimens were assumed to achieve a similar initial saturation level after one month of acclimatisation in laboratory conditions. The epoxy covering edges was assumed as contributing insignificantly to specimen water absorption, since it was degassed in a vacuum chamber. The remaining moisture in the specimens was removed by placing samples in an oven for 24 hours drying period at 50°C. After the drying period, specimens were cooled in a sealable bag and then placed in water, taking measurements every 24 hours. The water absorption tests continued until two consecutive measurements produced similar results. At this point, it was concluded that the specimens reached moisture equilibrium.

Fig. 1 presents the average values with maximum positive and negative deviation describing the process of water absorption (in % of the specimen dry mass) in the 2 mm and 4 mm specimens. The level of water absorption at 144 and 168 hours after the beginning of the tests was similar in each specimen. Given that the maximum length of cavitation erosion tests was 3 hours, it was decided that a sufficient level of moisture equilibrium was reached. The average water absorption at 168 hours was 0.248% in the 2 mm thick specimens and 0.161% in the 4 mm thick specimens. The maximum deviation from the average value was under 0.04

% in the 2 mm thick specimens and under 0.02% in the 4 mm thick specimens. It is important to note that the 2 mm and 4 mm thick specimens absorbed similar quantities of water (in grams). This resulted in the nearly doubled percentile water absorption of 2 mm thick specimens due to the twice smaller dry specimen mass.

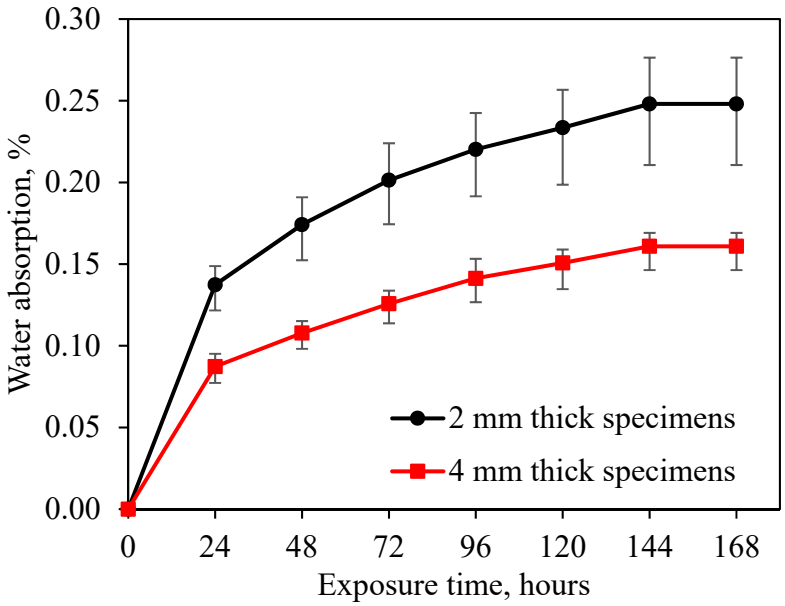

Fig. 1. Evolution of water absorption over time for 2 mm and 4 mm thick GFRP specimens with epoxy covered edges. The data is shown in average values with maximum positive and negative deviations.

An ultrasonic transducer Bandelin HD3200 was used in all erosion tests. This transducer operates at a frequency of 20 ± 0.5 kHz, and its maximum peak to peak amplitude with a TT13 probe tip is 165 µm. In the calibration of the erosion intensity adequate for the specimens used, the peak to peak amplitude was initially set to 25 µm and then gradually increased to 50 µm in accordance with ASTM G32 [7]. The 50 µm peak to peak amplitude was further used in all the cavitation erosion tests.

A resonant radius (R_r) of a bubble produced by an ultrasonic field can be calculated by the Minnaert resonance equation [17]:

$$R_r = \sqrt{\frac{3\gamma P_A}{\rho(2\pi f)^2}} \quad (1)$$

where γ is the heat capacity ratio, P_A is the ambient pressure, ρ is the water density and f is the frequency. For a 20 kHz frequency ultrasonic field, Eq. (1) yields R_r = 160 μm. Note that Eq. (1) neglects surface tension and viscous attenuation. However, the experimental measurements of cavitation bubble radiuses in 20 kHz ultrasonic field made by Bai et al. [18] and Feng et al. [19] agree with the numerical estimation provided by Eq. (1).

The schedule of specimen measurements (i.e., weighing, microscope observations and photographing of the erosion imprint) in all conducted tests consisted of two first measurements taken at 5 minutes intervals, followed by measurements at 10 minutes intervals. This method enabled the monitoring of the initial damage of the material surface and the determination of governing parameters. In each measurement pause, the specimen surface was cleaned with ethanol, which led to evaporation of water from pits and grooves in the erosion imprint. Additionally, the surface was dried with non-linting absorbent cloth, which is a standardised drying procedure in water absorption tests (e.g. ASTM D5229/D5229M [15]). The specimen surfaces were examined for remains of cloth fibres before weighing. Given a large number of measurement pauses, the applied drying procedure was found to be more time-efficient than the use of a desiccator and eliminated the uncertainty related to the surface and absorbed water removal. The mass of the specimen (m) was measured on scales with ±0.1 mg precision.

The erosion imprint was examined and photographed using a microscope Olympus GX71, as well as photographed with a digital camera under enhanced lighting. Additionally, several specimens were scanned before the exposure to cavitation and all specimens were scanned

after the tests using Micro-CT. The images of eroded areas were analysed with the image processing software ImageJ [20] and VGStudio Max [3].

The cumulative mean depth of erosion (MDE) was calculated by taking specimen mass loss (Δm) during cavitation erosion, specimen density (ρ) and eroded surface area (A), as shown in Eq. (2):

$$\mathrm{MDE} = \frac{\Delta m}{\rho A} \tag{2}$$

The specimen acoustic impedance (z) was measured in accordance with the ASTM E494 [21] standard using two 5 MHz transducers Sonatest SLH5-10, function/arbitrary waveform generator Keysight 33220A and an oscilloscope Keysight DSO-X 2004A. The ultrasonic wave velocity (v) was calculated by dividing specimen thickness by wave propagation time. The specimen thickness was measured with a calliper (with ±0.01 mm precision) and ultrasonic wave propagation time was measured with an oscilloscope. A single probe technique was found to be inadequate due to the low signal strength. Instead, a two-probe technique was applied, where the first transducer was used as a signal emitter and the second as a signal receiver. The transducers were placed on the opposite sides of the specimen in a tank filled with water with 23 °C. The amplitude of the first transducer was set to 10 V_{pp}. The frequency of the function/arbitrary waveform generator, where a single burst cycle was generated, was set to 5 MHz. The second transducer measured the delay of the signal transmitted though the specimen. The applied system was calibrated in water. The two-probe technique demonstrated high accuracy, as shown in Table 2. As can be seen in the table, the values of the speed of sound (v) and the acoustic impedance (z) are consistent for specimens cut from the same GFRP sheets. The specimens from sheet 2 have the lowest FVF and therefore the lowest ρ and z, while the specimens from sheet 3 have the highest. The FVF and

ρ of the specimens from sheet 2 were similar to those from sheet 4. However, the average value of v was by 14.7% larger in the sheet 4 leading to a larger z (by 18.7%).

2.3. Ultrasonic transducer calibration

The calibration of the transducer operation was performed using the stationary cavitation erosion testing method (ASTM G32 [7]) and two Stainless Steel 316 (SS316) specimens. Specimen 1 was eroded for 12 hours, while the test of specimen 2 had to be stopped at 4.5 hours because of the severe wear of the transducer tip which started to affect the erosion process. Fig. 2 depicts the measured data together with the data from ASTM G32 [7]. As can be seen, the average measured MDEs fall within the range of standard values [7]. It should be noted, however, that the data given in the standard omits the incubation period for SS316 and is averaged.

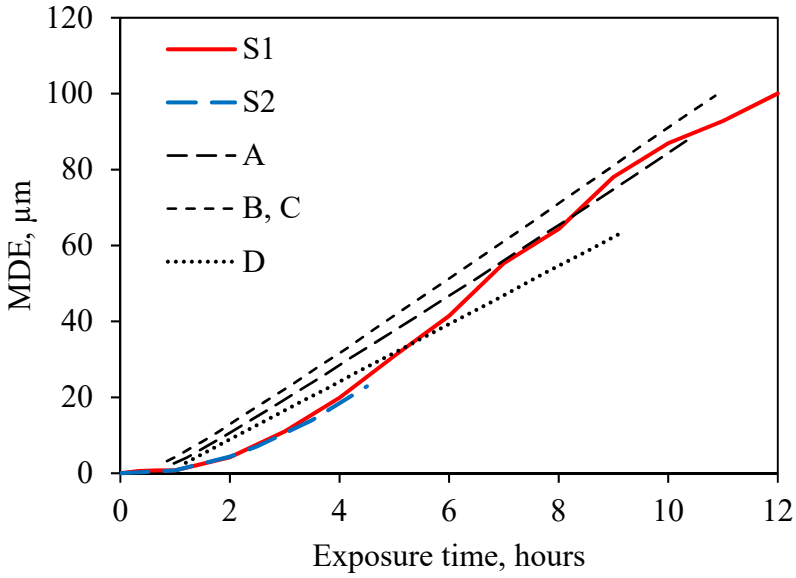

Fig. 2. Evolution of the mean depth of erosion (MDE) over time for Stainless Steel 316 exposed to ultrasonic cavitation. S1 and S2 are measured in this study. A, B, C and D are taken from Fig. X3.1 of ASTM G32 [7].

3. Results and discussion

3.1. GFRP specimen erosion

Cavitation erosion tests were performed on eight specimens, two from each GFRP sheet. The observations of the erosion imprints showed that the eroded area was oval and covered 84.3 mm^2 (σ = 3.03 mm^2). The shape of the erosion imprint was similar to the shape of the transducer tip TT13 but had smaller dimensions. The average eroded area was 8.4 mm in width and 11.2 mm in length, while the tip was 10 mm in width and 12.7 mm in length. This difference was caused by a hemispherical shape of the cavitation cloud on the transducer tip and a set distance of 0.8 mm from the tip to the specimen surface. The pressure in the cavitation cloud was maximum at the 0.8 mm distance from the transducer tip based on the acoustic field pressure measurements. The cavitation cloud created by the transducer eroded the tip face as well. Fig. 3 demonstrates four erosion stages of the tip face with the exposure time increasing from left to right. The erosion initiated at the tip edge and propagated inside, eventually covering the whole face. The highest damage developed around the tip edge, see the right image. This phenomenon occurred due to the central bolt-type connection of the removable tip to the transducer. This connection allowed for more intense vibration of the free tip edges casing more aggressive localised cavitation. A similar surface erosion pattern was observed by Fatjó et al. [22] on a tip with a circular face. The GFRP specimens also exhibited higher damage on the perimeter of erosion imprint, especially during the initial erosion stage.

Fig. 3. Erosion stages of the face of TT13 ultrasonic transducer tip. Damage increases with cavitation exposure time from left to right. Each image shows a 10 mm × 12.7 mm area. The images show from left to right the cavitation exposure times of 30 minutes, 120 minutes, 500 minutes and 1990 minutes.

The results of the erosion tests in terms of cumulative MDE and mass loss vs. exposure time are depicted in Fig. 4 for the GFRP specimens. The values of the MDE (in μm) are given by the left ordinate, while the values of the mass loss (in mg) are given by the right ordinate. As can be seen, Stainless Steel 316 (Fig. 2) outperformed significantly the GFRP composite (Fig. 4).

The development of erosion damage in the 2 mm thick specimens (i.e. the specimens 11, 12, 21 and 22) was similar. On the other hand, the 4 mm thick GFRP specimens reached significantly higher MDE during the same erosion time and specimens from different sheets (i.e. the specimens 31 and 32 compared to the specimens 41 and 42) demonstrated different rates of damage accumulation. The 2 mm thick specimens began eroding after 10 minutes of exposure, whereas the 4 mm thick specimens showed signs of erosion already after 5 minutes. The 2 mm thick specimens demonstrated a stable increase in the MDE and mass loss with time after a distinct incubation period of approximately 15 minutes. The 4 mm thick specimens demonstrated rapid MDE evolution over the initial erosion period without any significant incubation. After 10 minutes of cavitation erosion, the average MDE of the sheet 1 specimens was equal to 0.3 μm, the sheet 2 specimens to 0.6 μm, the sheet 3 specimens to 15.5 μm and the sheet 4 specimens to 7.8 μm. The average MDE values increased to 50 μm, 51.4 μm, 138.2 μm and 73.9 μm, respectively, by 100 minutes of testing. These results indicate that during the initial 10 minutes the specimen erosion differed twice for specimens from different composite sheets with similar thickness. After 100 minutes of erosion, the MDE in the specimens from sheet 3 was 87% higher than in the specimens from sheet 4, whereas the MDE of the specimens from sheets 1 and 2 differed only by 2.8%.

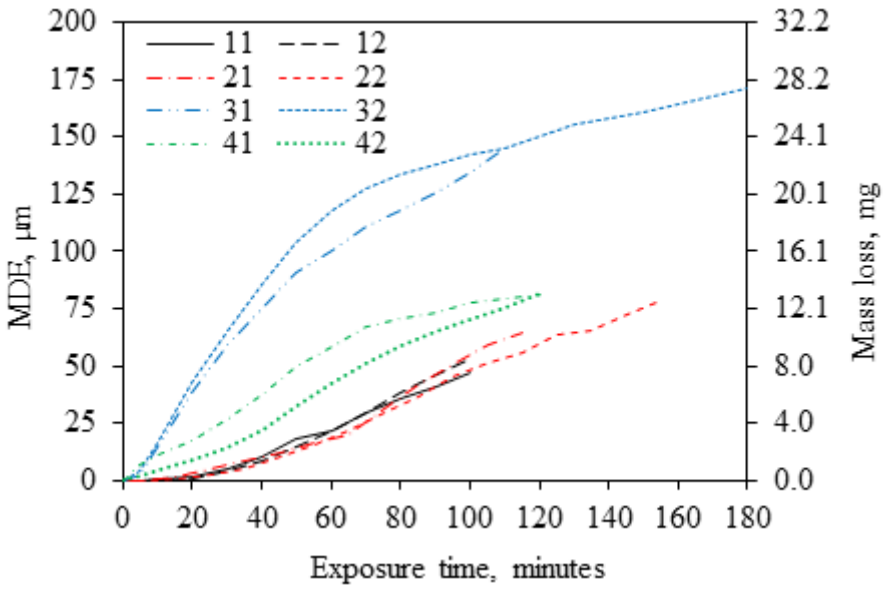

Fig. 4. Evolution of the cumulative mean depth of erosion (MDE) and mass loss over time for GFRP composites exposed to ultrasonic cavitation. The values of the MDE (in µm) are given by the left ordinate. The values of the mass loss (in mg) are given by the right ordinate.

The 87% difference in the MDE (at 100 minutes of erosion) of the specimens from the sheets 3 and 4 corresponded to the 1.9% difference in the acoustic impedance (z). The 160% difference in the MDE of the specimens from the sheets 3 and 1 corresponded to the 16.8% difference in z. On the other hand, a 3.9% difference in z of the specimens from the sheet 1 and 2 did not have any significant effect on the MDE. Therefore, the relationship between the MDE and z is nonlinear. It should be noted that z is measured for an entire specimen (see Section 2.2), while the erosion process has a localised nature controlled by the bundle layup and the quality of the manufacturing process.

The bundles in the surface lamina of the 4 mm thick specimens were closely packed (had smaller gaps) and had thinner epoxy covering layer, see Figs. 14-17, which led to a higher content of glass fibres at the surface. Since the glass fibres are harder and more brittle than the epoxy, the surfaces of the 4 mm thick specimens were overall harder and more brittle than those of the 2 mm thick specimens. This was also indicated by the Shore hardness measurements, which were slightly higher for the 4 mm thick specimens (see S_B and S_E values

in Table 2). As a result, the 4 mm thick specimens underwent higher erosion damage (higher MDEs).

The specimens from sheet 3 eroded faster than the specimens from sheet 4, which can be the result of the following factors. First, microscope observations showed that surfaces of the specimens from sheet 3 contained larger and more numerous initial defects (scratches, indentations, non-covered fibres). Second, Micro-CT scanning showed that the surface bundles of the specimens from sheet 4 had rounder edges that those from sheet 3 (see Figs. 16 and 17). The epoxy-filled gaps between the surface bundles of the specimens from sheet 4 were 50% wider than in the specimens from the sheet 3, and the epoxy layer covering the bundles was thicker. All these resulted in higher fibre content in the surfaces of the sheet 3 specimens. Thus, surface scratches and indentations facilitated the nucleation of cavitation bubbles thus leading to erosion initiation, while higher fibre content made the surface harder, more brittle and thus more susceptible to cavitation erosion.

The erosion rate, calculated by dividing the cumulative MDE by the exposure time, is presented in Fig. 5. The figure shows that the 2 mm thick specimens had relatively similar cumulative erosion rates, whereas the 4 mm thick specimens demonstrated greater differences. Overall, the thicker specimens eroded significantly faster than the thinner ones.

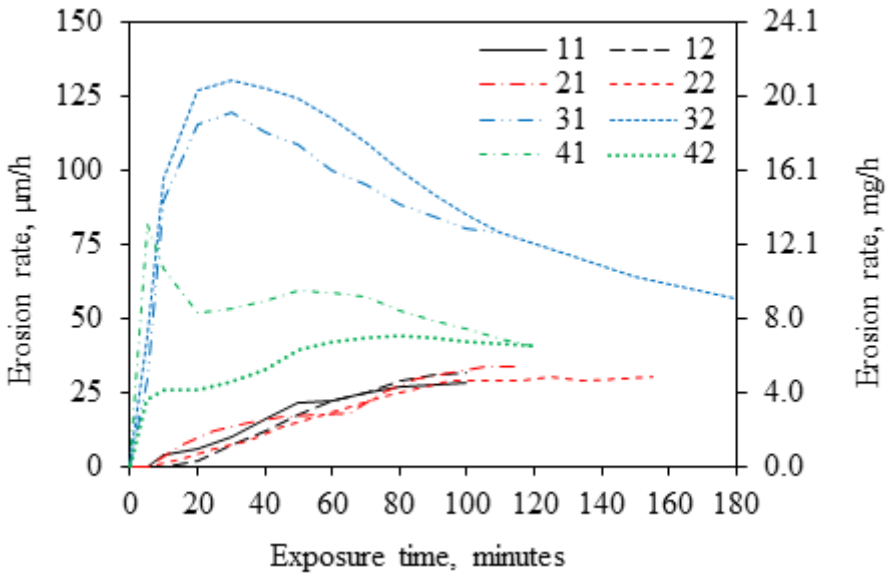

Fig. 5. Evolution of the cumulative erosion rate over time for GFRP composites exposed to ultrasonic cavitation. (Calculated as MDE / t). The values of the erosion rate (in µm/h) are given by the left ordinate. The values of the erosion rate (in mg/h) are given by the right ordinate.

All the 4 mm thick specimens showed a distinct initial period of accelerated erosion, which lasted 5 minutes in the specimen 41 (with erosion rate reaching 82.0 µm/h), 10 minutes in the specimen 42 (with erosion rate reaching 26.1 µm/h) and 30 minutes in the specimens 31 and 32 (with erosion rates reaching 119.3 µm/h and 130.4 µm/h, respectively). The erosion rate gradually decreased in the specimens 31, 32 and 41, while it plateaued for 10 minutes in the specimen 42 and then continued increasing. Both specimens from sheet 4 showed a second acceleration stage beginning at 20 minutes. The erosion rate in the specimen 42 reached maximum at 80 minutes, after which it showed only a slight decrease. The erosion rate in the specimen 41 reached a second maximum at 50 minutes and then continued to fall, eventually coinciding with the specimen 42 at 120 minutes. The erosion rates in the 2 mm thick specimens developed similarly, reaching a maximum after 100 minutes of testing. On average, the maximum registered cumulative erosion rate of the 2 mm thick specimens differed by 7.1%, while of the 4 mm thick specimens by 98.5%.

To obtain a more detailed picture on the variation of the erosion process at different testing stages, the instantaneous erosion rate was calculated for each measurement interval as a ratio between the change in the MDE and the length of the time interval between two consecutive measurements (equal to 5 or 10 minutes). Fig. 6 demonstrates that all the 2 mm thick specimens experienced steady initial increase of instantaneous erosion rate. The maximum instantaneous erosion rate of the specimen 11 was equal to 44.7 μm/h at 50 minutes, of the specimen 12 to 55.9 μm/h at 80 minutes, of the specimen 21 to 67.1 μm/h at 75 minutes and of the specimen 22 to 52.2 μm/h at 95 minutes. The maximum instantaneous erosion rates of the 2 mm thick specimens were significantly smaller than those of the 4 mm thick specimens and occurred later. The specimens 31 and 32 showed an initial sharp acceleration of the erosion (reaching 149.1 μm/h at 10 minutes and 156.5 μm/h at 20 minutes, respectively) followed by fast decline of the instantaneous erosion rate. The specimens 41 and 42 had two distinct stages of erosion acceleration. The instantaneous erosion rate of the specimen 41 reached 82.0 μm/h at 5 minutes during the first acceleration stage and 74.5 μm/h at 50 minutes during the second. The first peak in the instantaneous erosion rate of the specimen 42 was much lower, reaching only 29.8 μm/h at 10 minutes, while the second peak reached 67.1 μm/h at 50 minutes. On average, the maximum erosion rate per measurement for the 2 mm thick sheets differed by 18.5%, while for the 4 mm thick sheets by 105%. The instantaneous erosion rates of all specimens stabilised after approximately 80 minutes of testing, although fluctuations were present.

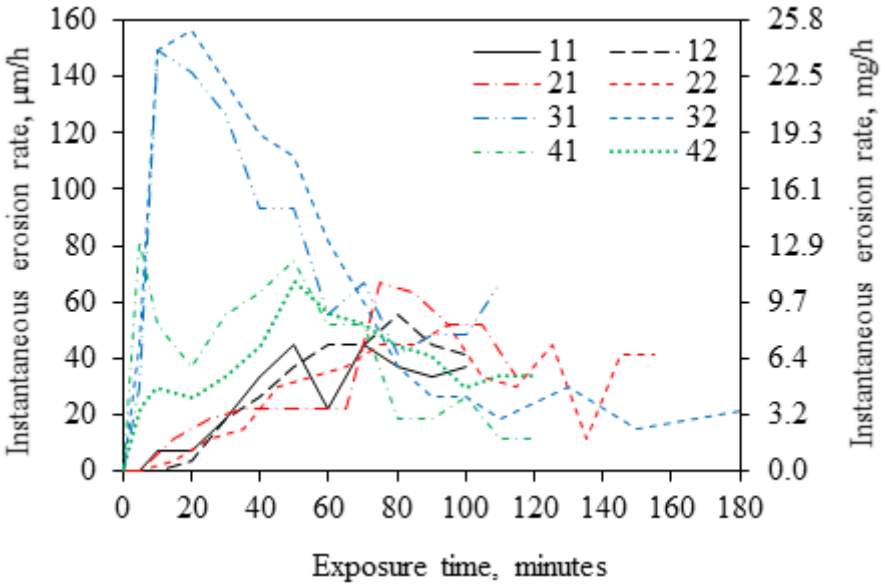

Fig. 6. Evolution of the instantaneous erosion rate over time for GFRP composites exposed to ultrasonic cavitation. (Calculated as ΔMDE / Δt). The values of the instantaneous erosion rate (in µm/h) are given by the left ordinate. The values of the instantaneous erosion rate (in mg/h) are given by the right ordinate.

3.2. Comparison with existing studies

The tests presented here were performed on GFRP composites with fibres laid up in unidirectional bundles. FRP laminates are complex composite materials, cavitation erosion performance of which depends on several geometrical and material properties. The effects of fibre type, fibre bundle layup, epoxy type and specimen thickness are examined hereafter by comparison with the existing studies on ultrasonic cavitation erosion of various FRP composites.

Hammond at al. [1] investigated the resistance of E-Glass/5920, Scotch Ply 1002, AS4/APC-2 and IM7/997-2T to ultrasonic cavitation. Only the specimens conditioned in salt water were used for comparison with the new results. The specimen thickness was 6 mm. E-Glass/5920 was made of E-Glass fibres in the woven roving layup bonded by rubber toughened epoxy, Scotch Ply 1002 of E-Glass fibres in the 0/90 layup bonded by epoxy, IM7/997-2T of carbon fibres in the 0/90 layup bonded by thermoplastic polymer (PEEK) and AS4/APC-2 of carbon

fibres in the +45/90/-45/0 layup bonded by thermoplastic toughened epoxy. The peak to peak amplitude of the ultrasonic transducer tip was 25 µm, which was 50% smaller than in the current research. The acoustic impedance was about 1.9 times higher than in the specimens used in the current research. The MDE values from Hammond at al. [1] tests are shown in Fig. 7. The MDE at 100 minutes of erosion of Scotch Ply 1002 was about 20% smaller than the average MDE of the 2 mm thick specimens from the current study. The rubber toughened epoxy increased the erosion resistance of E-Glass/5920 at 100 minutes of testing by 3.7%. AS4/APC-2 eroded significantly faster, with the MDE close to the one of the 31 and 32 specimens and showed an initial acceleration of the erosion process. IM7/997-2T demonstrated the highest erosion resistance at 100 minutes of testing. E-Glass/5920, Scotch Ply 1002 and IM7/997-2T did not show any initial acceleration or incubation period.

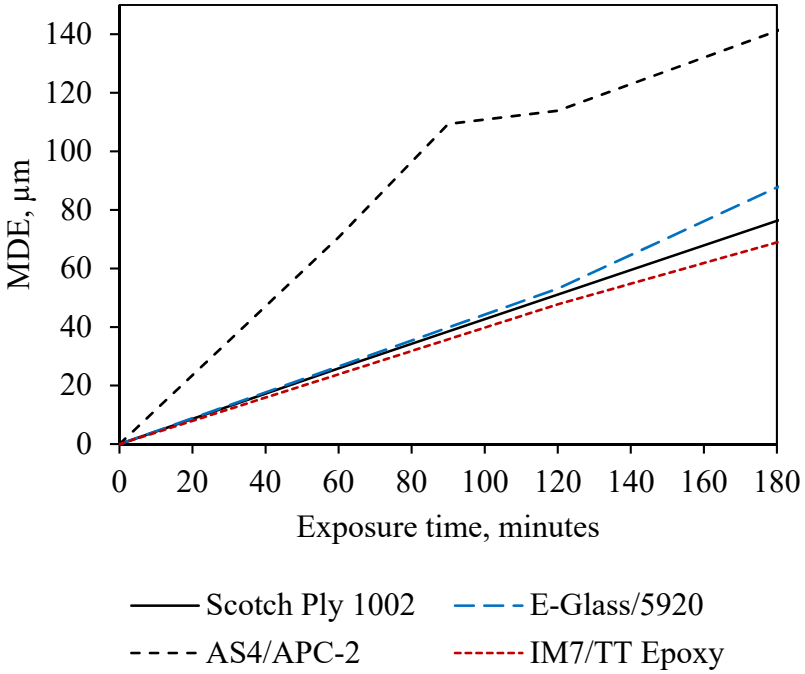

Fig. 7. Evolution of the mean depth of erosion (MDE) over time for FRP composites exposed to ultrasonic cavitation. The data is taken from Hammond et al. [1].

The tests done by Hammond at al. [1] differed from the tests done in this study in many parameters including material properties, internal layups of fibres and specimen thickness.

Additionally, the cavitation clouds in the new tests had higher aggressiveness due to higher peak to peak amplitude of the ultrasonic transducer tip. These differences hinder an accurate identification of the effect of any specific parameter on the process of cavitation erosion. It can only be deduced at this stage that the properties of the matrix are very important for the erosion resistance of FRP composites. Most of the specimens with the epoxy performed much better than those with the thermoplastic polymer (PEEK).

Yamatogi et al. [2] studied the resistance of several FRP composites to ultrasonic cavitation erosion at 50 μm peak to peak tip amplitude. The composites had glass, carbon or aramid fibres ('GF', 'CF' or 'AF' in specimen names, respectively), fabric or multiaxial layup ('Fab' or 'MA' in specimen names, respectively) and were fabricated using the vacuum assisted resin transfer moulding or prepreg autoclave method ('VaR' or 'Pre' in specimen names, respectively). Fibres in all specimens were bonded by epoxy. The Epoxy-VaR specimen was manufactured without any fibres. The thickness of all specimens was 2 mm. The erosion-induced mass loss was measured by a filtration technique, removing necessity of specimen preconditioning. Fig. 8 shows the results of Yamatogi et al. [2] tests together with the data for an epoxy-only specimen (EP2) from Hattori and Itoh [24]. The comparison of data in Figs. 4 and 8 shows that the specimens with glass and carbon fibres and the Epoxy-VaR specimen demonstrated higher (2-4 times) MDE than the maximum MDE obtained in the current research for the 4 mm thick specimen 32. The specimens with aramid fibres and the EP2 specimens behaved similarly to the 4 mm thick specimens 41 and 42. The GF-Fab-VaR specimen was the weakest in resisting erosion, showing the MDE of more than 630 μm after 100 minutes of testing.

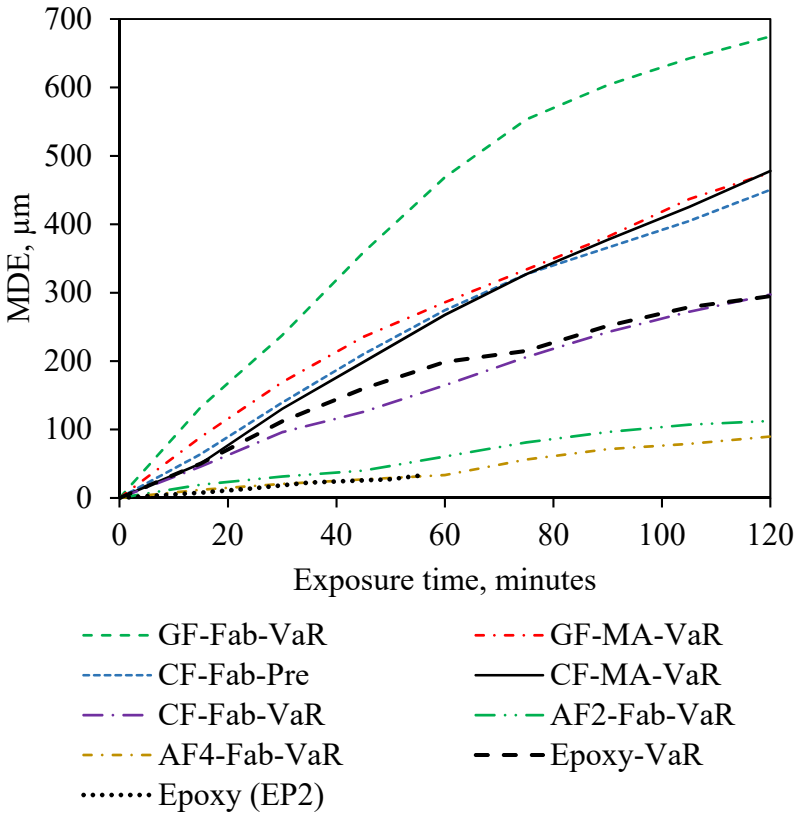

Fig. 8. Evolution of the mean depth of erosion (MDE) over time for FRP composites exposed to ultrasonic cavitation. The data is taken from Yamatogi et al. [2] and the EP2 data from Hattori and Itoh [23].

The analysis of data in Figs. 4 and 8 indicates that aramid fibres strengthened the specimens. The multiaxial layup strengthened the glass fibre specimens compared to the fabric layup but did not influence the carbon fibre specimens. The specimens with unidirectional glass fibre bundles investigated in this study showed superior erosion resistance. Since the erosion aggressiveness(produced by an ultrasonic transducer with 50 µm peak to peak tip amplitude) was similar in Yamatogi et al. [2] and this study, the better erosion performance can be attributed to the combined effects of better material properties and internal layups. Furthermore, a large difference between the epoxy-only specimens Epoxy-VaR and EP2 demonstrates the importance of epoxy properties on erosion resistance.

3.3. Erosion process

This section presents a detailed discussion of different stages of the cavitation erosion process observed in the tests. Several new erosion mechanisms have been identified. The surface erosion of specimens was monitored at regular intervals during testing through observations with a microscope and photography. Figs. 9-12 present a series of photographs (obtained by a microscope with 5× magnification) depicting nine stages of erosion development on a 2.6 mm × 3.5 mm area on the surfaces of the specimens 11, 21, 31 and 41, respectively. More detailed information of the surface erosion damage on the specimens can be obtained from the high-resolution photographs provided in the supplementary material. Erosion damage developed in different scenarios on each specimen, although several common mechanisms can be distinguished. The surfaces of each specimen had initial defects including scratches, indentations and individual shallow or partially uncovered fibres. These defects defined the regions of erosion initiation and its further accelerated development.

The erosion damage on the 2 mm thick specimen 11 initially concentrated around surface scratches and uncovered parts of individual fibres. The example of uncovered fibres is indicated in the image 1 of Fig. 9 by the left arrow, while the scratches are indicated by the right arrow. Multiple pits appeared around the scratches and new fibres were uncovered already after 5 minutes of cavitation exposure (see image 2). Cavitation deepened and widened the scratches. It is necessary to note that similar behaviour was reported elsewhere (e.g., [18, 24]). The fibres were further uncovered along their length with gradual removal of epoxy and widening of grooves, where fibres were located. Pits also developed in the regions without any significant initial defects, although the density of pits was low. By 30 minutes of exposure (image 5), more epoxy around the uncovered fibres was removed and the process of fibre removal began. The regions of fibre intersections were severely damaged and deeper fibres were exposed. The density of pits in the regions without any significant initial defects

increased. The process of fibre exposure and removal accelerated throughout testing. By 50 minutes of exposure (image 7), the surface of the specimen 11 was heavily pitted. Large portion of the surface epoxy was removed by 70 minutes of testing (image 9), while most of underlying fibres stayed covered.

The comparison between the images in Fig. 9 indicates that the erosion of the surface accelerated with time, which is represented by the increasing proportion of darker areas in the images. This conclusion is also supported by the accelerating growth of the MDE in Fig. 4 and the erosion rate profiles in Figs. 5 and 6.

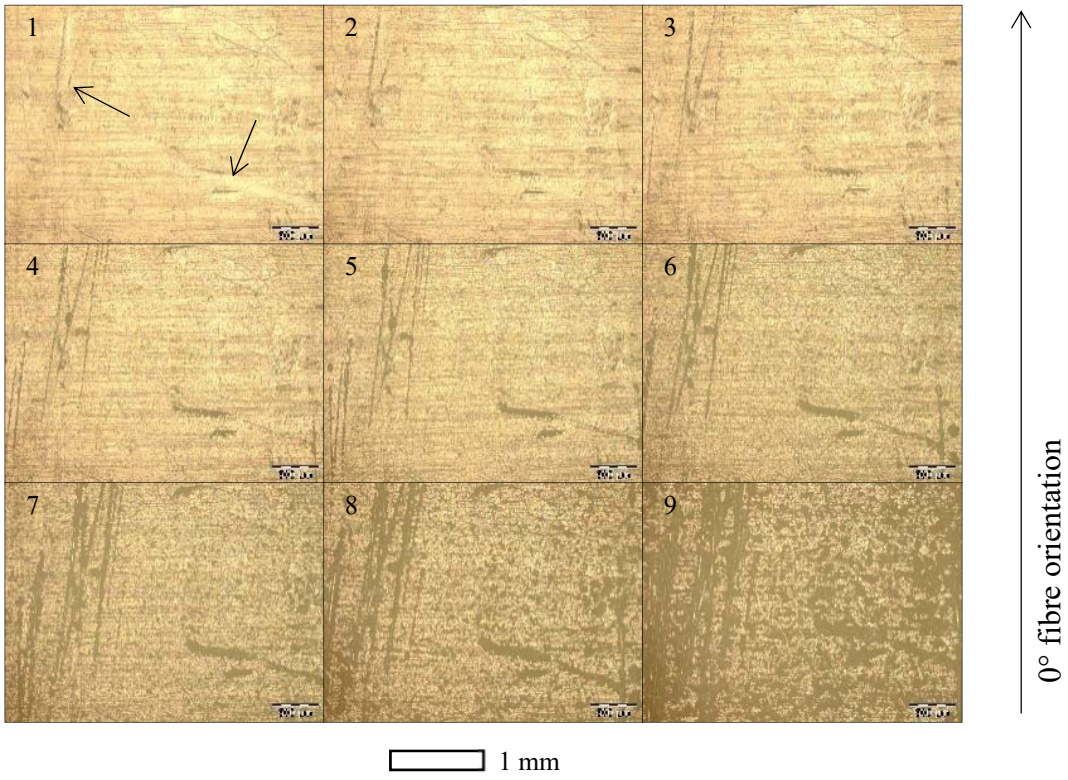

Fig. 9. Evolution of erosion damage in the specimen 11. Nine images depict the specimen surface at 0, 5, 10, 20, 30, 40, 50, 60, 70 minutes of exposure to ultrasonic cavitation. The images were originally obtained with 5× magnification. The bar at the bottom represents 1 mm. High resolution images are provided in the supplementary material.

The 2 mm thick specimen 21 had a fibre bundle with several fibres located close to the surface (indicated by the top arrow in the image 1 of Fig. 10) and a cluster of deep surface

scratches (indicated by the bottom arrow). First pits appeared on the surface already at 5 minutes of exposure. After 15 minutes of exposure, several surface fibres were uncovered in the top right corner of the image 2, while the scratches in the cluster were extended, widened and deepened. The process of fibre exposure continued, fibre removal was observed after 25 minutes (image 3), the scratches merged into a cavity, whose bottom reached the fibre bundle. The process of localised burrowing into the surface trough a cavity is characteristic of FRP composites. It was first referred to as the 'tunnelling' effect [1] and is generated by the experimental setup. The driving mechanisms of the tunnelling effect include (i) cyclic loading of the cavity bottom and walls by the pressure waves created by the transducer, (ii) pumping of water impregnated with bubbles into the cavity, and (iii) nucleation of bubbles inside the cavity. The mechanisms (i) and (ii) produce the 'wave guide' effect [1]. By 35 minutes (image 4), a large area of epoxy was removed above the fibre bundle. Multiple fibres were removed from the bundle in the exposed area and in the cavity. The rest of the surface was also heavily pitted. By 55 minutes (image 5), the tunnelling continued, the cavity was further widened and deepened with a localised removal of deeper fibres. By 65 minutes (image 6), the cavity merged with the damaged area at the top. The tunnelling effect caused severe localised removal of fibres, unmatched in other eroded areas. It created a deep cut of about 700 μm long in the bundle. By 95 minutes (image 9), all the initial surface epoxy was removed, and a deep tunnel was developed through the bundle at the location of the cavity. Additionally, the exposed fibre bundle developed many deep trenches, possibly due to a mechanism similar to the tunnelling effect (see Section 3.4 for discussion).

The comparison between the images in Fig. 10 suggests that the erosion process in Fig. 10 accelerates sufficiently after 65 minutes of testing (compare image 6 with images 7-9). This erosion acceleration corresponds to the accelerating growth of the MDE in Fig. 4. There is

also an increase in the erosion rate in Fig. 5 after 65 minutes of exposure and a jump in the instantaneous erosion rate in Fig. 6.

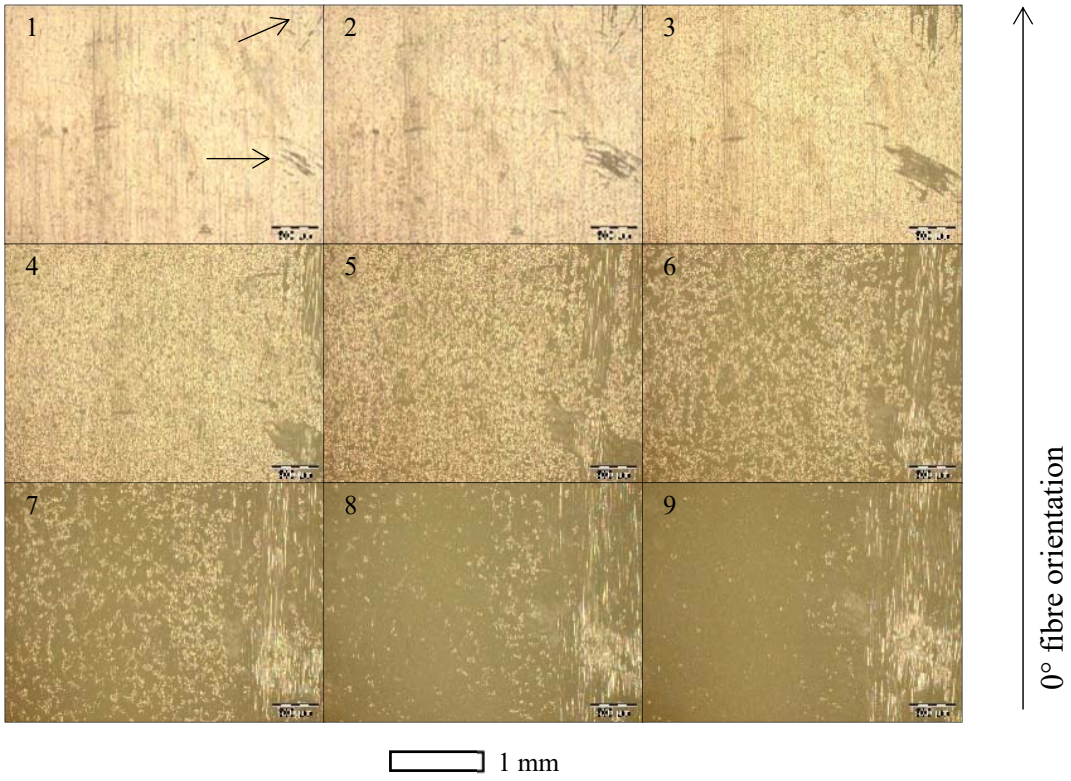

Fig. 10. Evolution of erosion damage in the specimen 21. Nine images depict the specimen surface at 5, 15, 25, 35, 55, 65, 75, 85, 95 minutes of exposure to ultrasonic cavitation. The images were obtained with 5× magnification. The bar at the bottom represents 1 mm. High resolution images are provided in the supplementary material.

The 4 mm thick specimen 31 had many deep initial grooves in the epoxy above the fibre bundle on the right of the arrow, which is positioned over the epoxy-filled gap between two bundles in the image 1 of Fig. 11. The presence of grooves led to a large area of epoxy being removed already after 5 minutes of cavitation with the exposure of many fibres (see image 2). Additionally, an inclined binding synthetic thread in the epoxy between the bundles was uncovered. Pits covered the remaining epoxy, but their density was low. By 10 minutes (image 3), most of the bundle was uncovered and fibre removal began. Part of the inclined

binding synthetic thread in the epoxy between bundles was removed as well. By 20 minutes (image 4), both bundles from both sides of the epoxy-filled gap were uncovered and many fibres were removed. Most of the thread in the epoxy-filled gap was also removed. The top of the epoxy remaining above the gap was covered by a relatively dense net of pits. Fibre removal continued throughout the test and the remaining epoxy band became narrower, exposing more fibres. The newly exposed fibres were located deeper in the epoxy due to the rounded corners of the bundles. Once the epoxy ridge developed, its erosion occurred in a different mechanism. The bottom part of the ridge wall was eroded first creating overhangs, which were chipped off at a later stage. Deep trenches were also observed on the exposed surface of the bundles. The ability of ultrasonic cavitation erosion to borrow into pit walls was previously reported by Hammond at al. [1]. In their tests, the erosion tunnelled into the IM7/997-2T specimen surface between fibre bundles and then removed epoxy resin from under the bundles.

A remarkable feature of the erosion process of the specimen 31 is that the thin epoxy layer and top bundle fibres were rapidly removed creating valleys, while the epoxy above the gap between the bundles remained even after 70 minutes of cavitation exposure (see image 9). As a result, a relatively intact epoxy ridge was created between two valleys of significantly eroded fibre bundles. Similar behaviour was observed in other specimens (see Section 3.4 for further experimental evidence). This observation is supported by the findings of Hammond at al. [1], who reported that the epoxy in the gaps between rovings of E-Glass/5920 was damaged less than the rest of the surface. However, the other three FRP composites (i.e., Scotch Ply 1002, AS4/APC-2 and IM7/997-2T) experienced initial removal of the epoxy between and under fibre bundles followed by the erosion of bundles themselves. E-Glass/5920 and Scotch Ply 1002 were manufactured using E-Glass fibres, whereas AS4/APC-2 and IM7/997-2T had carbon fibres (see Section 3.2). The resin type was different in all

specimens. This indicates that cavitation erosion of the resin between bundles depends on its properties (i.e., hardness and brittleness) rather than on fibre type or bundle layup.

The comparison between the images in Fig. 11 indicates that the erosion process depicted in Fig. 11 accelerates until 30 minutes of exposure (see images 1-5), which corresponds to the rapid increase in the MDE in Fig. 4 and the initial erosion rates in Figs. 5 and 6. After 30 min, the changes between the images 6-9 are not that significant, indicating a certain slowing down of the process.

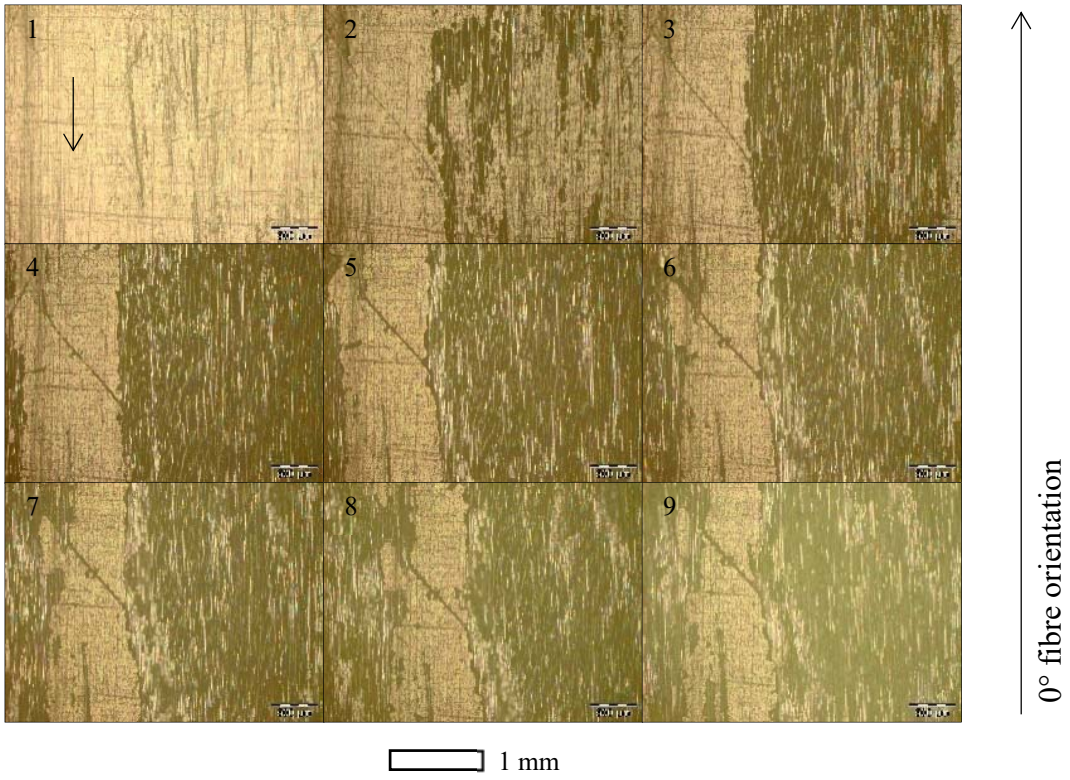

Fig. 11. Evolution of erosion damage in the specimen 31. Nine images depict the specimen surface at 0, 5, 10, 20, 30, 40, 50, 60, 70 minutes of exposure to ultrasonic cavitation. The images were obtained with 5× magnification. The bar at the bottom represents 1 mm. High resolution images are provided in the supplementary material.

The surface of the 4 mm thick specimen 41 was covered by a net of surface scratches and indentations. Additionally, there were fibres close to the surface in the region indicated by the right arrow in the image 1 of Fig. 12. The erosion initiated and localised in both regions indicated by the arrows in the image 1. By 5 minutes of testing several fibres were exposed in the low right corner of the image 2, while the epoxy in the top middle region developed multiple elongated grooves through widening, extending and deepening of small surface scratches. A low-density net of pits appeared on the epoxy. By 10 minutes (image 3), the existing grooves deepened and connected, while more fibres were uncovered. By 20 minutes (image 4), the groves connected into a trench, showing evidence of the tunnelling effect. The bottom of the trench did not reach the fibres yet. More fibres were exposed at the bottom right corner and fibre removal began. The net of pits on the epoxy surface became denser. The tunnelling trench widened, reached the underlying fibre bundle by 30 minutes of exposure (see image 5) and the top fibres were cut. Larger area of epoxy was removed above the fibre bundle at the bottom of the area examined. Fibre removal continued with deeper fibres being exposed. By 40 minutes (image 6), the tunnelling effect in the trench led to the development of a deep, long, narrow cut through the bundle. The trench widened further, exposing larger area of the bundle. The area of the uncovered bundle at the bottom of the image 6 extended towards the trench. The net of pits on the epoxy surface was very dense. The trench connected with the eroding area by 60 minutes of testing (image 8). By 70 minutes (image 9), the trench further extended, widened, deepened and developed two distinct deep tunnels in the cut. Furthermore, the exposed bundle at the bottom of the examined area developed deep trenches.

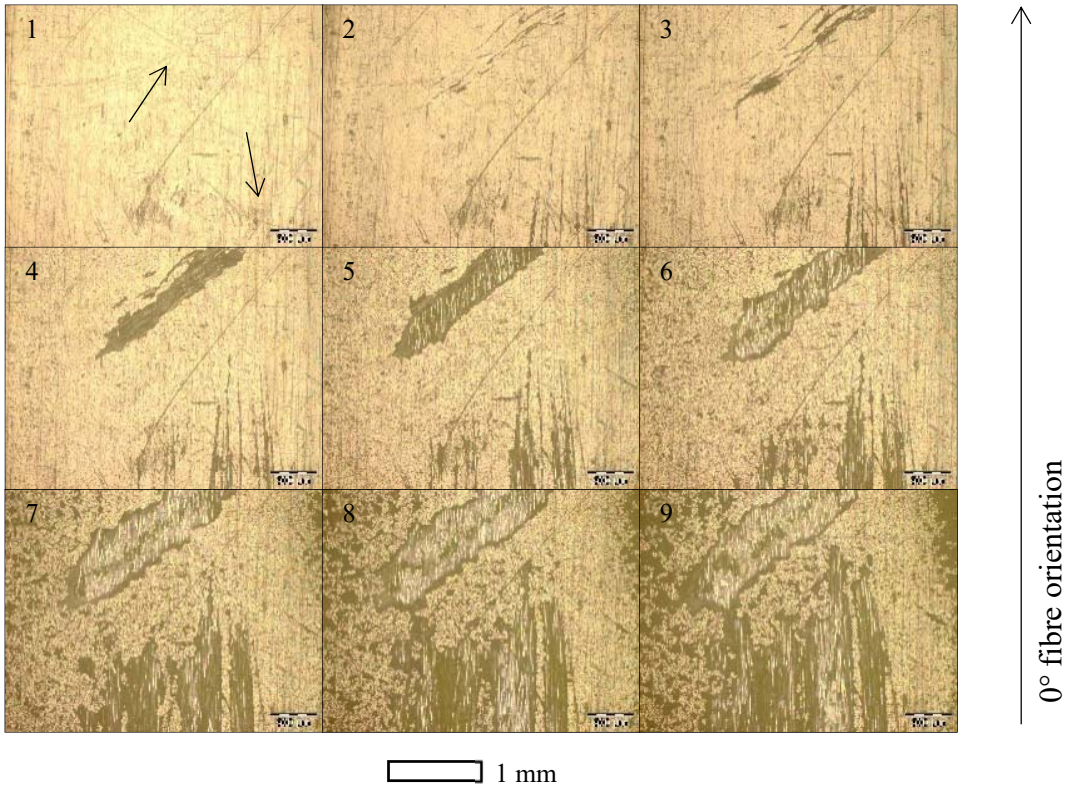

Fig. 12. Evolution of erosion damage in the specimen 41. Nine images depict the specimen surface at 0, 5, 10, 20, 30, 40, 50, 60, 70 minutes of exposure to ultrasonic cavitation. The images were obtained with 5× magnification. The bar at the bottom represents 1 mm. High resolution images are provided in the supplementary material.

The comparison between the images indicates that the erosion process on the area shown in Fig. 12 developed gradually without any significant acceleration. The slowing down of the MDE growth in Fig. 4 and the decrease in the erosion rate with time in Figs. 5 and 6 are not distinguishable in the figure.

It is important to note that the photoelastic phenomenon was observed in all specimens at the ends of many broken fibres still embedded in the composite, which indicated the presence of residual strain caused by the applied deformations. Note that it was possible to see this phenomenon because the microscope, employed in this study, used polarised light for specimen illumination. To observe photoelasticity, look for a rainbow effect at the ends of

broken fibres in heavily eroded areas shown in the high-resolution images of Figs. 9-12 (provided in the supplementary material).

The specimen 41 was used for more detailed examination of the mechanisms involved in the epoxy erosion. Fig. 13 presents a series of photographs (obtained by a microscope with 100× magnification) depicting six stages of erosion development in a 98 μm × 127 μm area on the specimen surface. The considered area of the specimen 41 was initially covered with a net of scratches and indentations clearly visible in the image 1 of Fig. 13. A detailed account of the surface erosion process is summarised henceforth. After 5 minutes of exposure, cavitation affected all the surface defects making them much more visible in the image 2. The largest indentation (indicated with an arrow in the image 1) was widened about 3 times and deepened, and three radial cracks extended from it. In addition, a deep pit appeared at a long, inclined scratch (indicated by an arrow in the image 2). The large increase in the indentation size and the double level structure of the pit bottom were caused by multiple nearby bubble collapses. After 10 minutes (image 3), the indentation grew further in size. The cracks emanating from the indentation extended and increased in number. The large pit on the left of the indentation deepened and widened. Additional pits with accompanying cracks appeared on the surface at the defects. After 20 minutes (image 4), the indentation and the existing pits continued to grow and deepen, new pits appeared. The scratches widened into grooves and their edges chipped off in many places. The existing cracks grew, new surface cracks appeared, making the net of cracks denser. A roughly rectangular region of epoxy between two scratches, indicated by an arrow in the image 4, was chipped off. A new erosion mechanism developed by 30 minutes of cavitation exposure. As can be seen in the image 5, surface cracks interconnected and extended to pits, separating pieces from the rest of the surface epoxy. These pieces were subsequently chipped off (e.g., see the cavity indicated by the arrow in the image 5). Additionally, the net of cracks became denser and the tunnelling

effect deepened existing cavities. The cavities were widened through erosion of walls and chipping of overhanging edges. The described erosion mechanisms accelerated by the 40 minutes of testing (see image 6). Similar material removal mechanisms were observed by Hattori and Itoh [23] during the cavitation erosion of homogeneous polymer materials.

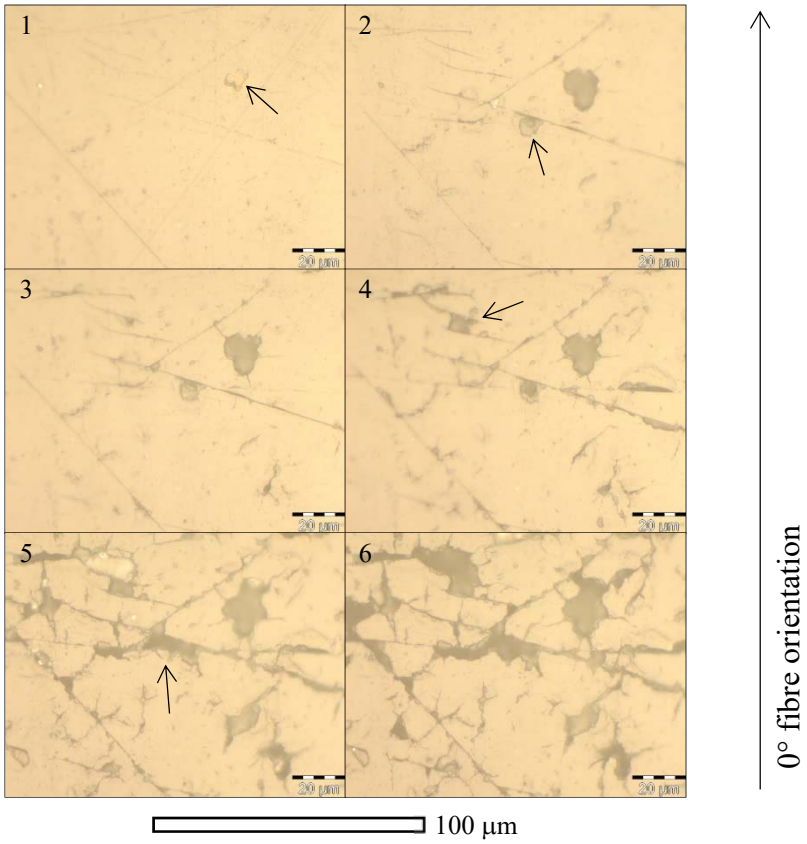

Fig. 13. Evolution of erosion damage in the specimen 41. Six images depict the specimen surface at 0, 5, 10, 20, 30, 40 minutes of exposure to ultrasonic cavitation. The images were obtained with 100× magnification. The bar at the bottom represents 100 µm. High resolution images are provided in the supplementary material.

The images of all erosion imprints at 5 minutes of cavitation exposure were analysed for the development of individual pits using the image processing software ImageJ [20]. It was assumed that each examined pit had a circular shape and was created by a single impact of a water jet generated by one collapsing bubble. The measured pits diameters varied from 0.7 to 3 µm. According to Philipp and Lauterborn [25] and Brujan et al. [26], the ratio between the

diameter of the water jet and the initial diameter of the bubble is approximately equal to 10. The resonant radius of the bubbles in the implemented testing conditions was 160 μm (see Section 2.2). Therefore, the diameter of the jet is about 16 μm. The comparison between the diameters of the jet and the examined pits yields the ratio between 5 and 23. In other words, there is a reduction in one order of magnitude between the initial diameter of the bubble and the diameter of the jet, and between the diameters of the jet and the pit, adding up to 2 orders of magnitude between the initial diameter of the bubble and the diameter of the pit generated.

3.4. Erosion imprint topography

The damage topography of the eroded surfaces was scanned using Micro-CT and analysed with the image processing software VGStudio Max [3]. Figs. 14-17 present the Micro-CT scans of the erosion imprints of the specimens 11, 21, 31 and 41, respectively. The figures include a top view of erosion imprint as well as horizontal and vertical cuts revealing erosion profiles. It is necessary to note that the erosion imprints of other specimens from same sheets were similar, showing analogous surface damage structures.

Fig. 14 depicts the eroded surface of the 2 mm thick specimen 11 after 100 minutes of cavitation exposure. The erosion imprint is shown in the top view by the brightest colour. Additional information about the layup of the fibre bundles (shown by the darkest colour), the location of the epoxy and the eroded profile can be easily obtained in the cuts.

The erosion imprint in the top view of Fig. 14 shows the development of heavy damage at the imprint perimeter and above fibres located close to the surface. The heavy damage around the erosion imprint corresponds well with the heavier erosion damage around the perimeter of the ultrasonic transducer tip (see Section 3.1 and Fig. 3). The erosion above the surface fibres led to the development of trenches, cross-sections of which are clearly visible in the top view and in the horizontal cut. The analysis of the Micro-CT images yielded the maximum erosion

depth of 314 μm, which was 6.7 times deeper than the MDE calculated for this specimen (see Fig. 4). The vertical cut (the cavity at the bottom of the eroded profile) shows the process of pit wall erosion, where the erosion burrowed into the wall at the pit bottom (see Section 3.3 for discussion of this process). The epoxy areas underwent pitting with distinct damage localisations at surface defects. There were some damage concentrations in the middle of the epoxy between bundles. However, the damage caused to the epoxy was much smaller.

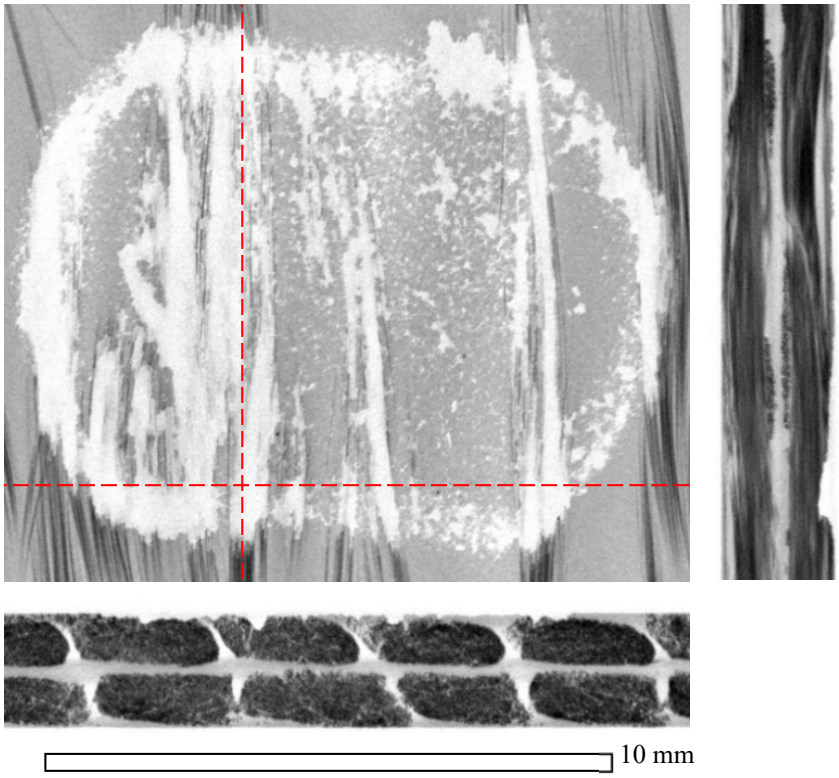

Fig. 14. Micro-CT images of the specimen 11 after 100 minutes of erosion. The horizontal cut is given on the right and the vertical below the top view. The locations of the cuts are indicted by the dashed lines. All images have similar scale. The bar at the bottom represents 10 mm. High resolution images are provided in the supplementary material.

Fig. 15 depicts the eroded surface of the 2 mm thick specimen 21 after 115 minutes of cavitation exposure. The comparison of the distribution of fibre bundles in the horizontal cuts in Figs. 14 and 15 shows that fibre bundles in the specimen 11 were narrower by about 27.7%

than those in the specimen 21, and the epoxy-filled gaps were larger. However, the fibre content in the surface layer was comparable and both specimens eroded at a similar rate.

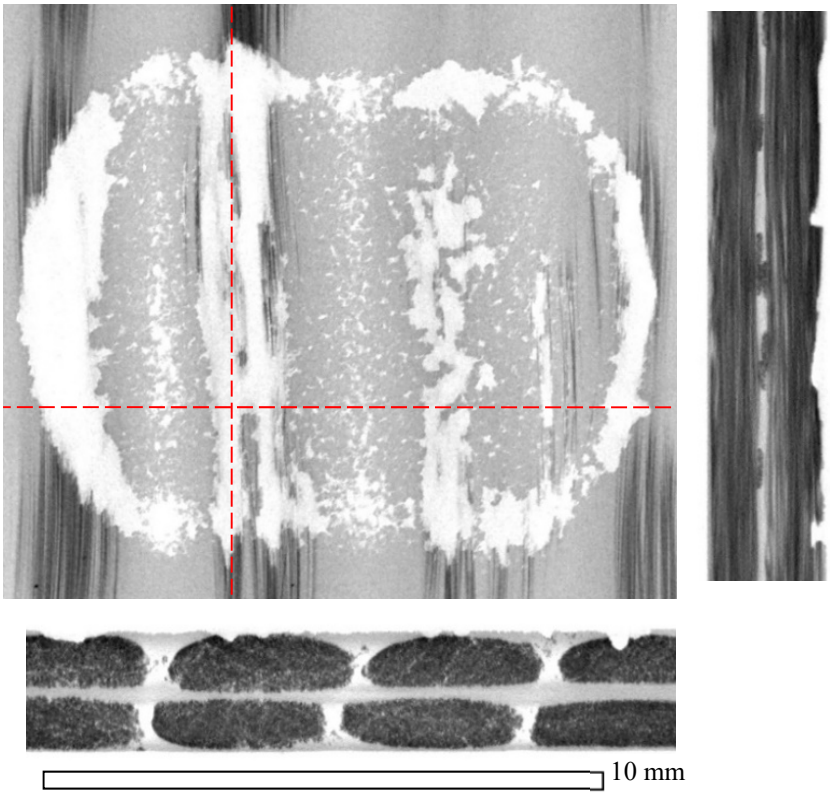

Fig. 15. Micro-CT images of the specimen 21 after 115 minutes of erosion. The horizontal cut is given on the right and the vertical below the top view. The locations of the cuts are indicted by the dashed lines. All images have similar scale. The bar at the bottom represents 10 mm. High resolution images are provided in the supplementary material.

The erosion imprint of the specimen 21 (see the top view of Fig. 15) also shows heavy damage at the imprint perimeter and above the surface fibres. The damage is much heavier where both cases coincide (see the left side of the imprint). Trenches developed above the surface fibres. The maximum erosion depth reached 385 μm, which was 6 times deeper than the MDE calculated for this specimen (see Fig. 4). The eroded pit walls with overhangs are clearly distinguishable in the vertical cut in the bottom pit. After the pit reached the depth of approximately 0.2 mm, the erosion started burrowing into the walls and creating overhangs. The overhangs would be chipped off at a later erosion stage. The epoxy areas underwent

pitting with some evident localisation in the middle of the epoxy between bundles, but the damage levels were much lower.

Fig. 16 depicts the eroded surface of the 4 mm thick specimen 31 after 110 minutes of cavitation exposure. It is evident that the specimen 31 developed a high level of surface damage because of a high erosion rate (see Figs. 4 and 5).

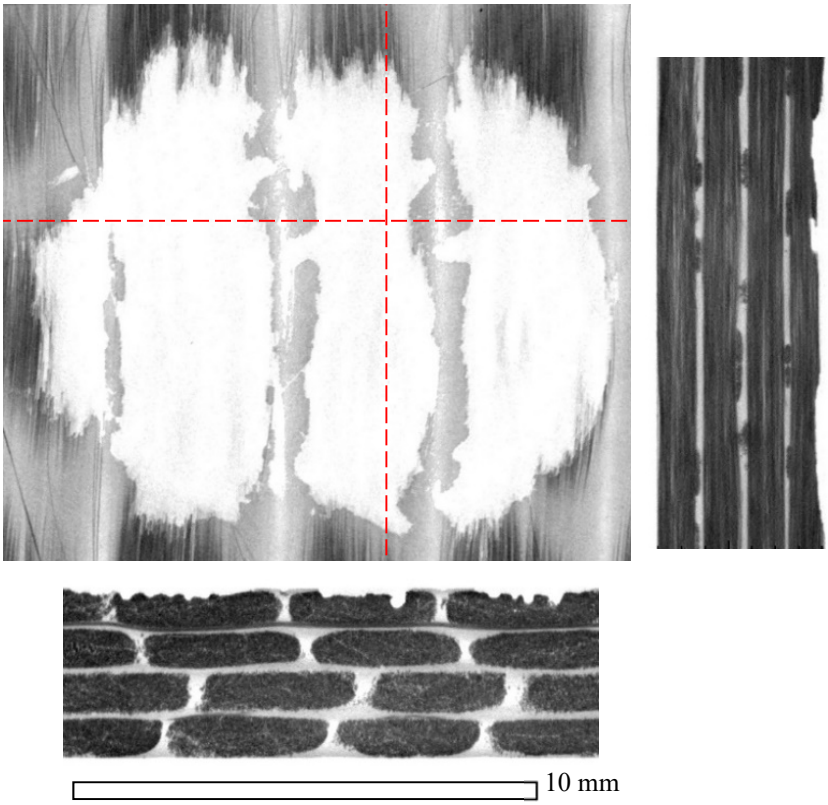

Fig. 16. Micro-CT images of the specimen 31 after 110 minutes of erosion. The horizontal cut is given on the right and the vertical below the top view. The locations of the cuts are indicted by the dashed lines. All images have similar scale. The bar at the bottom represents 10 mm. High resolution images are provided in the supplementary material.

The specimen 31 underwent considerable erosion above the bundles due to higher local hardness. Damage covered most of the erosion imprint and spread along fibres beyond the transducer tip perimeter (see the top view). The epoxy between bundles formed ridges protruding out of the eroded bundles. The tops of the epoxy ridges were pitted. The horizontal and vertical cuts show that trenches developed on the surfaces of eroded bundles due to

removal of whole bunches of fibres (see also Section 3.3 and Fig. 11). The process of erosion burrowing into pit walls and creating overhangs is clearly visible in the vertical cut. The maximum erosion depth reached 436 µm (the largest between the considered specimens), which is 3 times deeper than the MDE calculated for this specimen (see Fig. 4). The maximum erosion depth to MDE ratio for the specimen 31 is the smallest between the specimens considered in this section, despite that the specimen 3 had the largest maximum erosion depth. This is the result of the largest mass loss in this specimen (see Fig. 4).

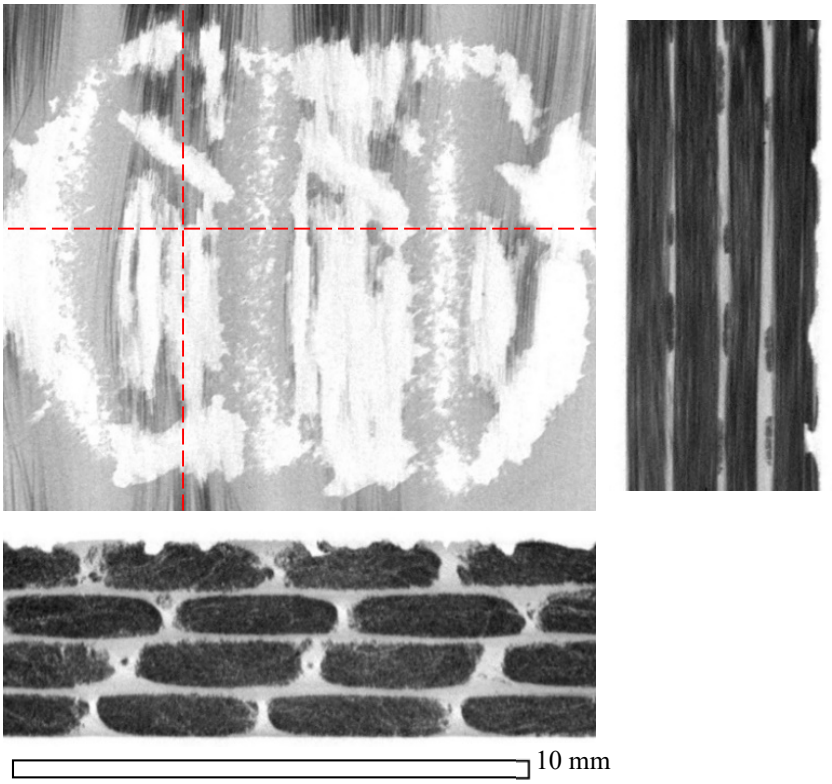

Fig. 17. Micro-CT images of the specimen 41 after 120 minutes of erosion. The horizontal cut is given on the right and the vertical below the top view. The locations of the cuts are indicted by the dashed lines. All images have similar scale. The bar at the bottom represents 10 mm. High resolution images are provided in the supplementary material.

Fig. 17 depicts the erosion surface of the 4 mm thick specimen 41 after 120 minutes of cavitation exposure. The erosion imprint displays the localisation effects of the erosion perimeter and fibre location on the erosion process. The surface above some shallow fibres

was only lightly eroded (see the top left part of the erosion imprint in the top view). The three inclined eroded trenches, visible in the top view, developed above binding synthetic threads located above fibre bundles in the cover epoxy layer. The erosion process proceeded with the tunnelling and trenching mechanisms. The maximum erosion depth reached 411 μm, which is 5 times deeper than the MDE calculated for this specimen (see Fig. 4). The overhangs created by erosion borrowing into pit walls are clearly visible in the horizonal and vertical cuts in Fig. 17. The overhang in the horizontal cut is severely undermined and ready to be chipped off. The epoxy between bundles underwent pitting, which was extensive in the middle of the gap.

It can be concluded that erosion acceleration occurred at the perimeter of the erosion imprint, above shallow fibres and at the uncovered bundles. The epoxy between bundles underwent only surface pitting. The erosion acceleration at the erosion imprint perimeter was caused by the central bolt-type connection of the removable tip to the transducer, which allowed for more intense vibration of the free tip edges and thus caused more aggressive cavitation. The inclusion of fibres changed the response of the surface to cavitation erosion. The epoxy layer above fibre bundles had a stiffer substrate than that located between bundles. This is evident from the Shore hardness measurements (S_B and S_E) given in Table 2. The fibres disrupted homogeneity as well as hardened and embrittled the surface. This caused stress concentrations, microcracking, and thus large damage developed at shallow fibres and synthetic thread in the surface epoxy. The erosion in the regions where the bundles were uncovered was more extensive than where the bundles were covered by a thick epoxy layer. These observations contradict the findings of Hammond et al. [1], who reported that the epoxy between bundles eroded first. The high erosion damage at uncovered bundles was the result of high hardness and brittleness of glass fibres and chipping of whole bunches of fibres. Based on these observations, it can be deduced that a thicker surface epoxy layer can mitigate

cavitation damage. The differences in the erosion mechanisms emphasise the importance of fibre bundle layup for the erosion performance of FRP composites.

As can be seen in the horizontal cuts in Figs. 16 and 17, the surface fibre bundles of the 4 mm thick specimens 31 and 41 had flattened cross-sections, thin epoxy covering layer and close packing (small epoxy-filled gaps between bundles). As a result, the specimen surfaces had a higher fibre content. This conclusion is supported by large areas of bundles visible on the undamaged surfaces shown in the top views. The cross-sections of the surface fibre bundles of the 2 mm thick specimens, visible in the horizontal cuts in Figs. 14 and 15, were more oval, had thicker epoxy cover and wider gaps between bundles. This resulted in a lower fibre content in the specimen surfaces. Therefore, the 4 mm thick specimens had harder and more brittle surfaces and underwent heavier erosion. The specimen 31 had the most eroded surface with the deepest pits, even though the specimens 21 and 41 had longer cavitation exposure.

It is necessary to note that the SS316 specimens eroded quite uniformly without any significant erosion localisation. At an advanced erosion stage, distinguishable pits formed on the steel surface, but with quite even distribution over the whole eroded surface. Therefore, the MDE is suitable for the assessment of the damage level in the SS316. On the other hand, the GFRP specimens eroded unevenly due to their heterogeneous anisotropic inner structure, brittle nature and presence of surface defects leading to high localisation of erosion damage. The tunnelling and trenching effects led to the maximum erosion depths that were much greater (up to 6.7 times) than the MDE approximation. Therefore, the MDE cannot reflect the nonuniformity of the erosion imprint and may be an inefficient parameter for the assessment of the erosion damage in GFRP composites exposed to ultrasonic cavitation.

4. Conclusions

In this research, unidirectional glass fibre reinforced polymer (GFRP) composites were tested for the resistance to ultrasonic cavitation erosion. Specimens were cut from four sheets with different fibre bundles/epoxy distribution and two thickness groups (2 mm and 4 mm). The cavitation erosion tests were conducted according to the ASTM G32 [7] standard. The erosion imprints were analysed with a microscope at regular periods and photographed. Additionally, X-ray computed microtomography (Micro-CT) scanning was performed after specimen testing. The analysis of test data yielded the following findings:

1. The structure of the removable tip (i.e. central bolt-type connection to the transducer) influenced the erosion imprint. The presence of the free tip edges caused higher erosion at the imprint perimeter.
2. The test results indicated that a highly nonlinear relationship exists between the mean erosion depth and acoustic impedance of GFRP composites. Further testing on GFRP composites with closely controlled layups is required before this relationship can be reliably established.
3. The specimen thickness affected the erosion process. After 100 minutes of exposure, the mean erosion depth of the 4 mm thick specimens was two times larger than that of the 2 mm thick specimens, while the maximum erosion rate of the thicker specimens was three times larger. The 4 mm thick specimens exhibited a period of initial erosion acceleration, while the 2 mm thick specimens exhibited a period of initial incubation.
4. The erosion process was highly influenced by the surface condition. Erosion initiated and localised around surface defects such as scratches, indentation, shallow and partially uncovered fibres.
5. Fibres hardened and embrittled surface epoxy, disrupted homogeneity and thus weakened its erosion resistance. Erosion concentrated over parts of fibre bundles located closer to

the surface creating trenches. Therefore, the shape of fibre bundle and the thickness of the epoxy cover are important factors for the erosion performance. The thinner the epoxy surface layer above the bundle, the higher the level of erosion damage developed.

6. The epoxy-filled gaps between bundles were less affected by erosion, creating protruding ridges on eroded surfaces. The tops of the ridges underwent surface pitting.
7. The findings of this research suggest that the optimisation of bundle layups (including bundle shape, packing and thickness of epoxy cover) together with fibre and epoxy material properties can be used for increasing erosion performance.
8. Several erosion mechanisms were observed. (i) The erosion burrowed locally into the surface creating vertical tunnels. A tunnelling pit could grow into a narrow cut across a fibre bundle. (ii) Long bunches of fibres were removed from exposed bundles creating trenches. (iii) After pits and trenches reached certain depth, the erosion burrowed into the bottom parts of walls creating overhangs. The overhangs were chipped off at a later erosion stage. (iv) The surface epoxy developed a net of interconnected cracks that separated pieces from the rest of the epoxy. These pieces were subsequently removed by cavitation.
9. A reduction in one order of magnitude exists between the initial diameter of the bubble and the diameter of the water jet, and between the diameters of the jet and the pit generated on the epoxy surface. Thus, the diameter of the pit is two orders of magnitude smaller than the initial diameter of the imploded bubble.
10. The depth of erosion imprints was highly uneven and the measured maximum erosion depth was much greater (up to 6.7 times) than the mean erosion depth calculated based on the mass loss. This raises questions about suitability of the latter parameter for the evaluation of erosion level in complex heterogeneous materials, such as GFRP composites, exposed to ultrasonic cavitation.

Acknowledgements

This research was supported by the Carnegie Trust (Dunfermline, UK) though RIG007459 grant, ÉireComposites Teo (Galway, Ireland), Centro Tecnológico de Componentes (CTC, Santander, Spain) and DEGIMA (Santander, Spain). The support is gratefully acknowledged.

References

1. Hammond, D., Amateau, M. and Queeney, R. Cavitation Erosion Performance of Fiber Reinforced Composites. Journal of Composite Materials 1993; 27(16): 1522-1544.
2. Yamatogi, T., Murayama, H., Uzawa, K., Kageyama, K. and Watanabe, N. Study on Cavitation Erosion of Composite Materials for Marine Propeller. In: Proceeding of ICCM-17 Conference. Edinburgh, July, 2009.
3. Volume Graphics. (2018). VGSTUDIO MAX: High-End Software for CT Data. [online] Available at: https://www.volumegraphics.com/en/products/vgstudio-max.html [Accessed 2 Aug. 2018].
4. BSI. BS EN ISO 1172:1999, Textile-glass-reinforced plastics. Prepregs, moulding compounds and laminates. Determination of the textile-glass and mineral-filler content. Calcination method., 1997.
5. Böhm, H., Betz, S. and Ball, A. The wear resistance of polymers. Tribology International 1990; 23(6): 399-406.
6. ASTM D2240 - 15e1, Standard Test Method for Rubber Property—Durometer Hardness. ASTM International, West Conshohocken, PA, 2015.
7. ASTM G32-16, Standard Test Method for Cavitation Erosion Using Vibratory Apparatus. ASTM International, West Conshohocken, PA, 2016.
8. Abdel-Magid, B., Ziaee, S., Gass, K. and Schneider, M. The combined effects of load, moisture and temperature on the properties of E-glass/epoxy composites. Composite Structures 2005; 71(3-4): 320-326.
9. Bian, L., Xiao, J., Zeng, J. and Xing, S. Effects of seawater immersion on water absorption and mechanical properties of GFRP composites. Journal of Composite Materials 2012; 46(25): 3151-3162.
10. Buehler, F. and Seferis, J. Effect of reinforcement and solvent content on moisture absorption in epoxy composite materials. Composites Part A: Applied Science and Manufacturing 2000; 31(7): 741-748.
11. Chow, W. Water absorption of epoxy/glass fiber/organo-montmorillonite nanocomposites. Express Polymer Letters 2007; 1(2): 104-108.

12. Ellyin, F. and Rohrbacher, C. The Influence of Aqueous Environment, Temperature and Cyclic Loading on Glass-Fibre/Epoxy Composite Laminates. Journal of Reinforced Plastics and Composites 2003; 22(7): 615-636.
13. Liao, K., Schultheisz, C. and Hunston, D. Long-term environmental fatigue of pultruded glass-fiber-reinforced composites under flexural loading. International Journal of Fatigue 1999; 21(5): 485-495.
14. Mourad, A., Abdel-Magid, B., El-Maaddawy, T. and Grami, M. Effect of Seawater and Warm Environment on Glass/Epoxy and Glass/Polyurethane Composites. Applied Composite Materials 2010; 17(5): 557-573.
15. ASTM D5229/D5229M-14, Standard Test Method for Moisture Absorption Properties and Equilibrium Conditioning of Polymer Matrix Composite Materials. ASTM International, West Conshohocken, PA, 2014.
16. ASTM D570-98(2010)e1, Standard Test Method for Water Absorption of Plastics. ASTM International, West Conshohocken, PA, 2015.
17. Minnaert, M. XVI. On musical air-bubbles and the sounds of running water. The London, Edinburgh, and Dublin Philosophical Magazine and Journal of Science 1933; 16(104): 235-248.
18. Bai, L., Xu, W., Zhang, F., Li, N., Zhang, Y. and Huang, D. Cavitation characteristics of pit structure in ultrasonic field. Science in China Series E: Technological Sciences 2009; 52(7): 1974-1980.
19. Feng, H., Barbosa-Cánovas, G. and Weiss, J. Ultrasound technologies for food and bioprocessing. New York: Springer, 2011.
20. National Institutes of Health (USA), 2018. Image processing software ImageJ. [online] Available at: https://imagej.nih.gov/ij/ [Accessed 2 Aug. 2018].
21. ASTM E494-15, Standard Practice for Measuring Ultrasonic Velocity in Materials. ASTM International, West Conshohocken, PA, 2015
22. Fatjó, G., Torres Pérez, A. and Hadfield, M. Experimental study and analytical model of the cavitation ring region with small diameter ultrasonic horn. Ultrasonics Sonochemistry 2011; 18(1): 73-79.
23. Hattori, S. and Itoh, T. Cavitation erosion resistance of plastics. Wear 2011; 271(7-8): 1103-1108.
24. Dular, M. and Osterman, A. Pit clustering in cavitation erosion. Wear 2008; 265(5-6): 811-820.
25. Philipp, A. and Lauterborn, W. Cavitation erosion by single laser-produced bubbles. Journal of Fluid Mechanics 1998; 361: 75-116.
26. Brujan, E., Noda, T., Ishigami, A., Ogasawara, T. and Takahira, H. Dynamics of laser-induced cavitation bubbles near two perpendicular rigid walls. Journal of Fluid Mechanics 2018; 841: 28-49.